RSC Advances

PAPER

View Article Online
View Journal | View Issue

Cite this: *RSC Adv.*, 2026, **16**, 16358

Synergistic enhancement of hydrogen evolution reaction *via* N and Ni co-doping in TiO_2-modified Pt/C catalysts

Xufeng Lin, *[ab] Huijie Wei, [a] Yixuan Zhang,[a] Hua Chi,[a] Xiaofan Liu[a] and Yanyan Xi*[c]

Hydrogen production through water electrolysis represents a promising green pathway for future hydrogen generation. The development of catalyst materials capable of lowering the reaction energy barrier is crucial for improving electrolysis efficiency. This study synthesized a series of N and Ni co-doped Pt/TiO_2@C catalysts and systematically investigated the effects of N and Ni incorporation on their structure and electrocatalytic performance. Among them, Pt/TiO_2@1%Ni-N-C exhibited the optimal performance, with an overpotential as low as 84 mV and a Tafel slope of 115 mV dec^{-1}. Characterization results revealed the uniform distribution of Pt nanoparticles and the presence of an anatase TiO_2 crystalline phase. Increasing the Ni loading significantly enhanced the specific surface area of the catalysts while reducing the average pore size. Furthermore, N doping facilitated the anchoring and stabilization stabilizing of Ni atoms on the support. The strengthened interaction between pyridinic N and Ni atoms promoted the formation of Ni^+ species, which modulated the electronic structure of surface Ni and served as active sites for HER.

Received 5th March 2026
Accepted 19th March 2026

DOI: 10.1039/d6ra01906d

rsc.li/rsc-advances

1. Introduction

In recent years, the global energy crisis has intensified, which is largely attributable to the emission of hazardous gases from the combustion of traditional fossil fuels, which causes severe environmental damage.[1] Consequently, the development of clean, pollution-free renewable energy sources has become a major research focus. Hydrogen energy is particularly attractive due to its zero-emission nature, high energy density, and the abundance of raw materials.[2,3] Recent advances in heterogeneous catalysis have further expanded the possibilities for efficient hydrogen production through innovative catalyst design strategies.[4,5] Among various hydrogen production pathways, water electrolysis offer advantages such as rapid reaction rate and high product purity, positioning it as a promising primary method for future hydrogen generation.[6–8] However, the intermediate steps of the oxygen evolution reaction (OER) and hydrogen evolution reaction (HER) possess large kinetic barriers under ambient conditions.[9,10] Thus, designing efficient catalyst materials to reduce these energy barriers is essential for enhancing the overall performance of water electrolysis.

Pt-based catalysts are recognized as excellent HER catalysts, but their high cost and tendency for nanoparticle agglomeration at high Pt loadings limit their large-scale industrial application.[11,12] To reduce Pt usage, supported metal catalysts are commonly employed, where metal nanoparticles are dispersed on a high-surface-area support to improve mass-specific catalytic efficiency.[13] Carbon black is widely used as a support for Pt-based HER catalysts due to its high specific surface area and good electrical conductivity. Recent efforts have also explored the use of sustainable carbon sources, such as biomass-derived carbons, for catalyst support applications, demonstrating the potential for environmentally friendly catalyst design.[14] However, carbon supports are susceptible to corrosion under high potentials and during long-term operation in fuel cells, leading to Pt nanoparticle agglomeration, detachment, and performance degradation.[12,15,16] To address this issue, we modified the carbon support with metal oxide TiO_2, which exhibits superior chemical and electrochemical stability, thereby significantly enhancing the catalyst's durability.

Heteroatom-doped carbon materials represent a novel class of materials with unique electronic structures and chemical properties.[17] Nitrogen-doped carbon materials, in particular, have garnered widespread attention in catalysis. The similar atomic sizes of nitrogen and carbon minimize structural distortion of the carbon framework during doping, while the five valence electrons of nitrogen facilitate strong covalent

[a]*College of Chemistry and Chemical Engineering, China University of Petroleum (East China), Qingdao, 266580, P. R. China*

[b]*State Key Laboratory of Heavy Oil Processing, China University of Petroleum (East China), Qingdao, 266580, P. R. China*

[c]*Advanced Chemical Engineering and Energy Materials Research Center, China University of Petroleum (East China), Qingdao, 266580, P. R. China. E-mail: xiyy@upc.edu.cn*

bonding with carbon atoms.[18–20] When used as a support, N-doped carbon strengthens the metal–support interaction (MSI), thereby optimizing catalyst performance.[21] The high electronegativity of nitrogen also improves the electronic conductivity of the material. However, excessive nitrogen doping may lead to the collapse of the carbon skeleton.[19] The incorporation of nitrogen influences the catalyst in several ways: (1) it affects the nucleation and growth rates of active components during synthesis; (2) it modifies the interaction between active components and the support; (3) it alters the electronic structure of the metal.[22–25] Furthermore, nitrogen doping introduces defects into the carbon lattice, which can enhance the interaction between the carbon support and Pt nanoparticles.[26]

For the catalyst itself, the incorporation of nitrogen effectively modulates its overall acidity/basicity and wettability, thereby optimizing its activation capability toward reactants. The dispersion and stability of surface active components are also improved by nitrogen addition. Currently, N-doped carbon materials are extensively applied in various energy and environmental catalysis fields, including electrolysis and batteries.[18,27–30] Advanced *in situ* characterization techniques, such as Raman spectroscopy, have recently provided valuable insights into the dynamic behavior of catalyst surfaces during electrochemical reactions, further underscoring the importance of understanding structure–activity relationships at the molecular level.[31]

Nitrogen species in the carbon matrix can exist in several forms, including pyridinic N, pyrrolic N, graphitic N, and oxidized N (Fig. 1).[32] Pyridinic N possesses a lone pair of electrons capable of donating electrons, while graphitic N contributes to the conjugated system of the adjacent carbon structure.[33] The distribution of nitrogen species depends primarily on the doping method and temperature. As the doping temperature increases, the overall nitrogen content tends to decrease, with pyridinic and pyrrolic N decomposing preferentially, leaving the more stable graphitic N.[34–36]

Transition metal-based catalysts, including Ni, Co, and their derivatives, have attracted significant attention for electrocatalytic water splitting.[5,37] Ni species exhibit a unique capability to cleave water molecules, making them efficient co-catalysts for alkaline HER.[38,39] Moreover, Ni demonstrates higher stability compared to other metal oxides and hydroxides.[39–41] Compared with other transition metals (*e.g.*, Co, Fe, Cu), Ni offers a more favorable balance between water dissociation kinetics and cost-effectiveness, and has been widely demonstrated to form strong coordination with N-doped carbon supports, leading to enhanced metal–support interaction and charge redistribution.[42–44] These characteristics make Ni an ideal co-dopant for modulating the electronic structure and HER activity of Pt-based catalysts. It is noteworthy that Ni incorporation also influences the metal–support interaction within the catalyst, potentially inducing charge redistribution within the support.[39,41,45]

In this work, we employed TiO_2 to modify the carbon support, thereby enhancing its stability. Subsequently, N and Ni were introduced onto the support, followed by the loading of Pt as the active component, to systematically investigate the effects of N and Ni incorporation on the catalyst's structure and HER performance.

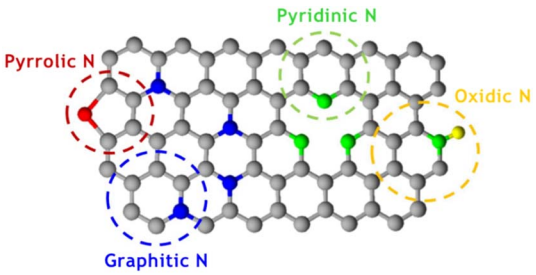

Fig. 1 Schematic diagram of nitrogen species in doped carbon structures.

2. Materials and methods

2.1 Experimental reagents and instruments

Carbon black was obtained by Cabot Corporation. Tetraethyl titanate, nickel nitrate hexahydrate ($Ni(NO_3)_2 \cdot 6H_2O$) and chloroplatinic acid hexahydrate ($H_2PtCl_6 \cdot 6H_2O$) were purchased from Sinopharm Chemical Reagent Co., Ltd. All liquid and solid materials used in this work have analytical purity, while all gaseous materials are of ultra-high purity (>99.99%).

2.2 Catalyst synthesis

2.2.1 Pretreatment of carbon black. Carbon black was acid-treated with a 1 : 5 (v/v) mixture of hydrochloric acid (HCl) and nitric acid (HNO_3) at 120 °C for 6 h. After natural cooling and standing overnight, the mixture was filtered under suction and washed 2–3 times with ethanol. The washed carbon black was dried in a vacuum oven at 80 °C for 4 h, followed by heat treatment at 500 °C for 4 h under an Ar atmosphere to remove excess surface hydroxyl groups.

2.2.2 TiO_2 modification of C support. A solution was prepared with tetraethyl titanate, hydrochloric acid, and ethanol with a volumetric ratio of 0.5 : 1 : 0.5. Then, 300 mg of carbon powder was added, and the mixture was ultrasonically dispersed at 60 °C for 2 h. A suitable amount of CH_3COOH was added to promote hydrolysis. After drying at 60 °C for 1 h, this mixture was left standing overnight. The resulting product was centrifuged, vacuum-dried at 80 °C for 3 h, and finally calcined at 500 °C for 4 h under Ar atmosphere to obtain the TiO_2@C support.

2.2.3 N-doping of TiO_2@C to obtain TiO_2@N-C. The TiO_2@C support was placed in a tube furnace, purged with Ar for 30 min to remove air, and then treated under an NH_3 atmosphere at 600 °C for 3 h.

2.2.4 Ni loading on TiO_2@N-C to obtain TiO_2@1%Ni-N-C and TiO_2@3%Ni-N-C. Solutions containing 1 wt% and 3 wt% Ni were prepared by dissolving $Ni(NO_3)_2 \cdot 6H_2O$ in 10 mL solvent. Then, 100 mg of the TiO_2@N-C support was added to

each solution, ultrasonicated for 1 h, and vacuum-dried at 80 °C for 24 h. The dried samples were calcined at 600 °C for 6 h under Ar atmosphere to obtain TiO_2@1%Ni-N-C and TiO_2@3%Ni-N-C supports.

2.2.5 Preparation of Pt/TiO_2@N-C, Pt/TiO_2@1%Ni-N-C, and Pt/TiO_2@3%Ni-N-C catalysts. The required mass of chloroplatinic acid hexahydrate ($H_2PtCl_6 \cdot 6H_2O$) was calculated based on a 20 wt% Pt loading. Then, 100 mg portions of TiO_2@1%Ni-N-C, TiO_2@3%Ni-N-C, and TiO_2@N-C were separately added to the H_2PtCl_6 solution, ultrasonicated for 20 min, stirred at 60 °C for 2 h, and left standing overnight. The products were centrifuged and washed the next day, followed by vacuum drying at 80 °C for 3 h.

2.2.6 Liquid phase reduction of catalysts. 100 mg of the Pt-loaded support was mixed with 4 mL of ethylene glycol and 6 mL of formaldehyde, and the mixture was stirred at 50 °C for 5 h to reduce the Pt precursors. The resulting catalyst was washed 2–3 times with ethanol and dried at 80 °C for 3 h.

2.3 Catalyst characterization

The detailed characterization process of these catalysts could be discovered in SI.

2.4 Performance evaluation of catalytic hydrogen evolution reaction

The detailed electrochemical measurements process of these catalysts could be discovered in SI. And the corresponding electrochemical measurement instrument was shown in Fig. S1, in SI.

3. Results and discussion

3.1 Basic physicochemical characterization

3.1.1 XRD analysis. X-ray diffraction (XRD) analysis was conducted to investigate the crystalline phases present in the catalysts, with careful attention to distinguishing between structural modifications resulting from doping and the formation of new crystalline compounds. Fig. 2 presents the XRD patterns of the Pt/TiO_2@3%Ni-N-C, Pt/TiO_2@1%Ni-N-C, and Pt/TiO_2@N-C catalysts. According to the ICDD PDF cards (No. 21-1272 and 21-1276), the diffraction peaks at 2θ = 25.3°, 37.8°, 48.1°, 54.5°, and 63° correspond to the (101), (004), (200), (211), and (204) crystal planes of anatase TiO_2, respectively.

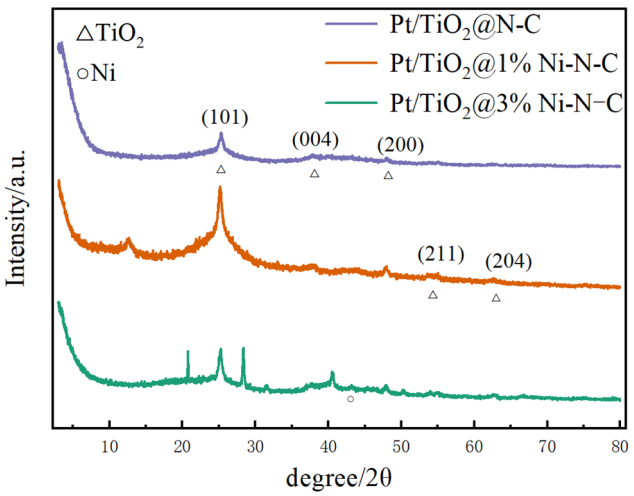

Fig. 2 XRD patterns of Pt/TiO_2@3%Ni-N-C, Pt/TiO_2@1%Ni-N-C, and Pt/TiO_2@N-C catalysts.

In the pattern of Pt/TiO_2@N-C, two distinct features are observed at approximately 13.0° and 27.4°. The peak at ~13.0° is characteristic of the (100) plane of graphitic carbon nitride (g-C_3N_4)-like structures, while the broad feature at ~27.4° corresponds to the (002) plane of graphitic carbon or nitrogen-containing carbon species. It is important to clarify that these features do not indicate the formation of a discrete new material such as a "metallic polymer" or a separate polymeric phase. Rather, they reflect the structural modification of the carbon support through nitrogen doping during NH_3 treatment, where nitrogen atoms are incorporated into the carbon framework, creating localized domains with structural characteristics resembling those of nitrogen-doped carbon materials.

Upon Ni doping, significant changes are observed in the XRD patterns. The peak at ~13.0° completely disappears in both Pt/TiO_2@1%Ni-N-C and Pt/TiO_2@3%Ni-N-C. This disappearance suggests that Ni atoms insert into the layered structure of the nitrogen-containing carbon domains, disrupting their long-range order and leading to their conversion into a more disordered N-doped carbon matrix. Concurrently, new peaks emerge at ~20.2° and ~27.4° in the Ni-doped samples. The peak at 20.2° corresponds to the (001) plane of β-$Ni(OH)_2$ (JCPDS No. 14-0117), indicating the presence of nickel hydroxide species formed during the synthesis. The peak at 27.4°, while still assignable to the (002) plane of graphitic carbon or residual nitrogen-containing carbon, exhibits broadening and intensity changes that reflect the structural modification induced by Ni incorporation into the carbon matrix.

With increasing Ni content, additional peaks appear at 2θ = 42.5°, 44.2°, 46.9°, and 52.4°. These are characteristic of metallic Ni in two crystal phases: the face-centered cubic (FCC) phase (peaks at 44.2° and 52.4° corresponding to the (111) and (200) planes) and the hexagonal close-packed (HCP) metastable phase (peaks at 42.5° and 46.9°). The emergence of these peaks confirms the successful loading of Ni onto the support, with Ni existing in multiple chemical states including metallic Ni^0 and β-$Ni(OH)_2$. The partial reduction of Ni species to metallic Ni^0 likely occurs through interaction with the carbon support during calcination.

Notably, a weak but discernible peak at ~40.0° is observed in all Pt-loaded samples, which corresponds to the (111) plane of face-centered cubic metallic Pt (JCPDS No. 04-0802). This peak confirms the successful loading of Pt nanoparticles onto the catalyst supports. The relatively low intensity of this peak may be due to the small particle size, high dispersion of Pt nanoparticles, or partial overlap with other reflections.

In summary, these XRD results demonstrate that NH_3 treatment leads to nitrogen doping of the carbon support, as evidenced by features resembling those of nitrogen-doped carbon structures. Ni incorporation disrupts the ordered

nitrogen-containing domains while introducing Ni-containing species including β-Ni(OH)$_2$ and metallic Ni—representing successful Ni loading rather than the formation of a separate polymeric phase from the carbon matrix itself. Pt remains in its metallic state, confirming successful catalyst preparation. The structural evolution observed by XRD directly supports our conclusion that Ni is successfully incorporated into the N-doped carbon matrix, modifying its structural order and creating the foundation for the synergistic effects observed in HER performance.

3.1.2 N_2 adsorption–desorption characterization. Fig. 3a displays the N_2 adsorption–desorption isotherms of the Pt/TiO_2@N-C series catalysts. All three samples exhibit type IV isotherms with H3-type hysteresis loops, indicative of mesoporous structures with irregular pore shapes. The dramatic increase in specific surface area upon Ni doping—from 7.8 m^2 g^{-1} for Pt/TiO_2@N-C to 108.9 m^2 g^{-1} for Pt/TiO_2@1%Ni-N-C and further to 135.2 m^2 g^{-1} for Pt/TiO_2@3%Ni-N-C—indicates substantial morphological evolution of the catalyst support. This enhancement, coupled with the relatively modest decrease in average pore size (from 8.8 nm to 4.3 nm), suggests that Ni incorporation promotes the formation of additional mesopores rather than simply enlarging existing pores. The pore size distribution curves (Fig. 3b) confirm this interpretation, showing that all Ni-doped samples exhibit pore sizes predominantly in the 10–15 nm range, regardless of Ni content.

As summarized in Table 1, high-temperature calcination under NH_3 atmosphere significantly increases the specific surface area of the catalysts but reduces the average pore size, suggesting the creation of new pores during this process. With increasing Ni content (from 1% to 3%), the average pore size further decreases, which might negatively affect mass transfer of reactants.

Such morphological changes have significant implications for catalytic performance. The increased surface area provides more sites for Pt nanoparticle dispersion, potentially leading to smaller Pt particles and higher active site density. The mesoporous structure (pores in the 10–15 nm range) is particularly advantageous for HER, as it facilitates efficient mass transport of reactants (water molecules and hydroxide ions) and products (hydrogen gas) while maintaining good accessibility to the active sites. The slight reduction in average pore size with increasing Ni content (from 4.3 nm to 4.1 nm) may represent a trade-off between surface area gain and mass transfer efficiency, which could explain why the 3% Ni-doped catalyst, despite having the highest surface area, does not exhibit the best HER performance.

Table 1 BET specific surface area and average pore size parameters of the catalysts

Catalyst type	Specific surface area (m^2 g^{-1})	Average pore size (nm)
Pt/TiO_2@N-C	7.8	8.8
Pt/TiO_2@1%Ni-N-C	108.9	4.3
Pt/TiO_2@3%Ni-N-C	135.2	4.1

3.2 TEM analysis

Fig. 4 and 5 show that the catalysts treated with NH_3 (excluding those with obvious encapsulation layers) exhibit enhanced structural stability and significantly improved electron storage capacity, which may be related to defect structures induced by the NH_3 treatment. In Pt/TiO_2@N-C, Pt nanoparticles are small, with sizes ranging between 12-22 nm. In Pt/TiO_2@1%Ni-N-C, Ni is predominantly enriched at the ends of the catalyst structure, which helps maintain the relatively stable size of Pt nanoparticles.

The TEM images (Fig. 4) provide visual confirmation of the morphological changes suggested by BET analysis. Pt/TiO_2@N-C (Fig. 4a and b) exhibits a relatively compact structure with limited porosity, consistent with its low surface area. In contrast, Pt/TiO_2@1%Ni-N-C (Fig. 4c and d) shows a more open, porous architecture with well-dispersed Pt nanoparticles, corroborating the high surface area and mesoporous nature revealed by BET. The Ni enrichment observed at the edges of the

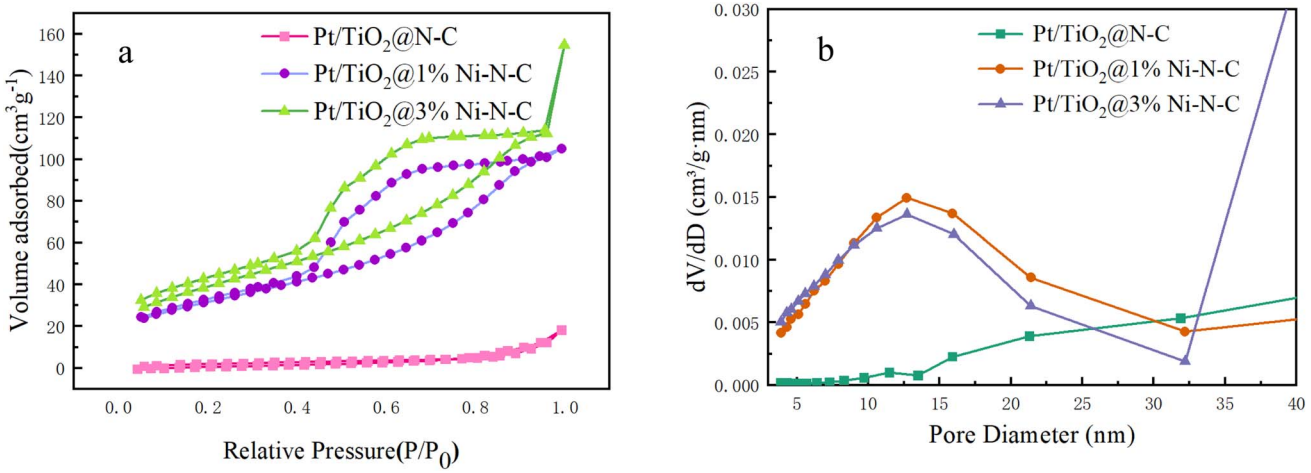

Fig. 3 Adsorption–desorption isotherms (a) and pore size distribution diagrams (b) of Pt/TiO_2@N-C series catalysts.

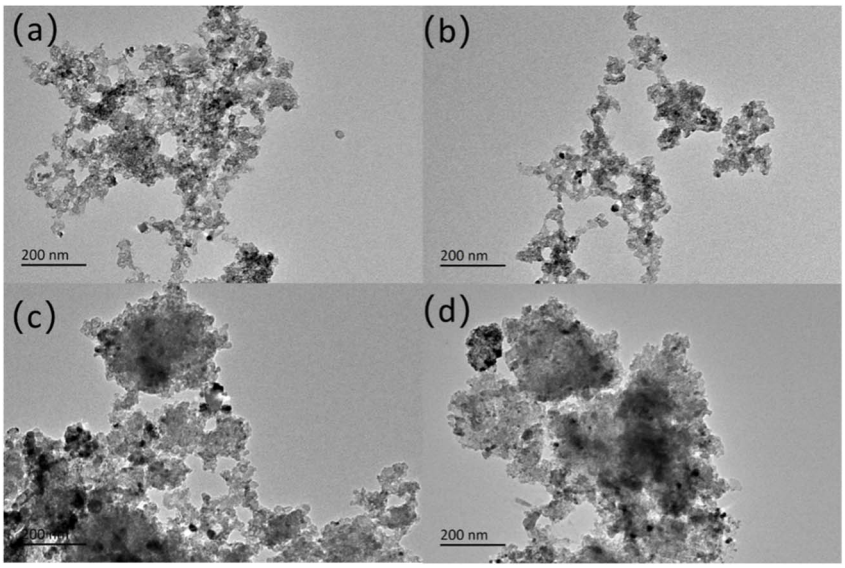

Fig. 4 TEM images of the Pt/TiO_2@N-C series catalysts: (a and b) Pt/TiO_2@N-C; (c and d) Pt/TiO_2@1%Ni-N-C.

catalyst structure in Pt/TiO_2@1%Ni-N-C may also contribute to the formation of additional pore channels during synthesis.

3.3 Spectroscopic study

3.3.1 Raman spectroscopy. Fig. 6 shows the Raman spectra of the catalysts. For carbon materials, the D band (1365–1405 cm^{-1}) is associated with vibrations of graphite rings and defects at grain boundaries, while the G band (1525–1570 cm^{-1}) originates from the sp^2 vibrations of carbon atoms (E_2g mode). The intensity ratio I_D/I_G reflects the degree of disorder in the carbon structure. Doping N atoms into the carbon layers disrupts the ordered sp^2 bonding of carbon, creating structural defects that can provide additional active sites for HER. However, excessive defects may lead to the collapse of the carbon matrix, reducing electrical conductivity.

After N doping, the D and G bands of the catalyst shift to lower frequencies with increased full width at half maximum (FWHM) and decreased total scattering intensity. This phenomenon can be attributed to two aspects: (1) the introduction of Ni atoms heterogenizes the carbon matrix, and the foreign atoms act as elastic scattering centers, reducing inelastic scattering signals; (2) the formation of chemical bonds between Ni and C/N atoms increases bond lengths and average atomic mass, collectively resulting in the redshift and broadening of D and G bands.

The I_D/I_G ratios are 0.973 for Pt/C, 0.994 for Pt/TiO_2@1%Ni-N-C, 0.945 for Pt/TiO_2@N-C, and 0.69 for Pt/TiO_2@3%Ni-N-C. These values reveal an important trend: moderate Ni doping (1%) actually increases defect density compared to N-doping alone, while excessive Ni doping (3%) significantly reduces defects. This non-monotonic behavior suggests that Ni plays a dual role—at low concentrations, it may create additional edge defects or structural distortions; at high concentrations, Ni aggregation or induced graphitization could heal defects or cover them.

Crucially, the HER activity does not simply follow the defect density trend. Pt/TiO_2@1%Ni-N-C (highest I_D/I_G) shows the best

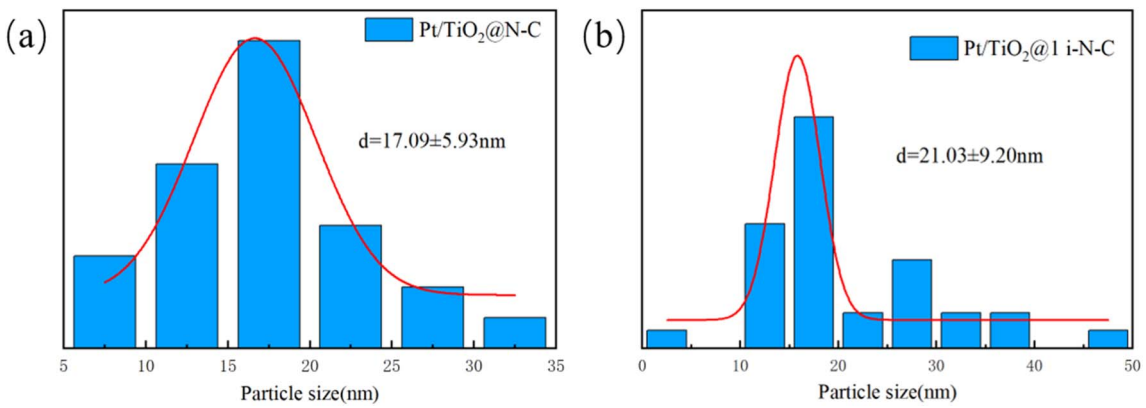

Fig. 5 Particle size distribution histograms of the Pt/TiO_2@N-C series catalysts: (a) Pt/TiO_2@N-C; (b) Pt/TiO_2@1%Ni-N-C.

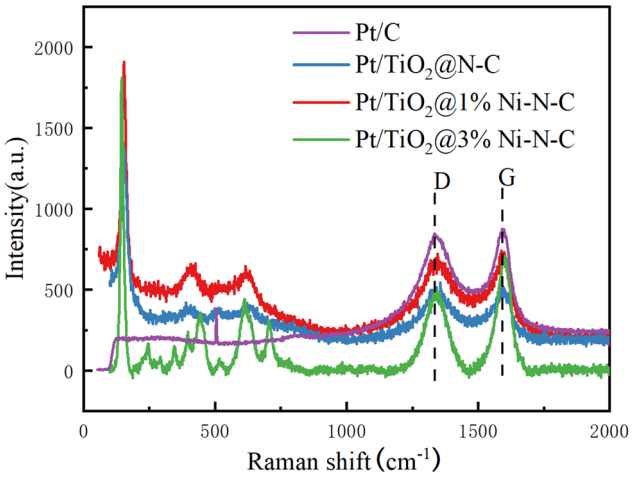

Fig. 6 Raman spectra of Pt/TiO_2@3%Ni-N-C, Pt/TiO_2@1%Ni-N-C, Pt/TiO_2@N-C, and Pt/C catalysts.

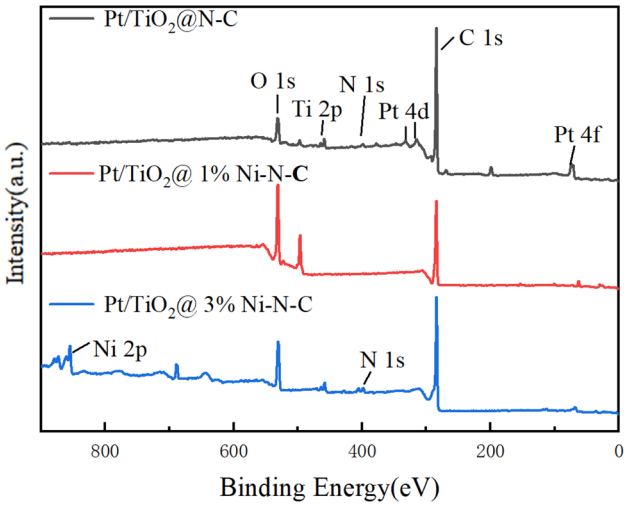

Fig. 7 XPS survey spectra of Pt/TiO_2@3%Ni-N-C, Pt/TiO_2@1%Ni-N-C, Pt/TiO_2@N-C, and Pt/C catalysts.

performance, but Pt/TiO_2@3%Ni-N-C (lowest I_D/I_G) still outperforms Pt/TiO_2@N-C (intermediate I_D/I_G). This indicates that while defects contribute to activity, they are not the dominant factor. Instead, the superior performance of Pt/TiO_2@1% Ni-N-C arises from an optimal synergy between moderate defect density (providing anchoring sites and electronic modulation) and the presence of Ni^+ species that effectively cleave H–OH bonds. The enhanced activity of Pt/TiO_2@3%Ni-N-C compared to Pt/TiO_2@N-C, despite its lower defect density, further confirms that Ni-mediated water dissociation plays a more decisive role than carbon defects alone.

Therefore, the Raman data should be interpreted as evidence of structural modification by N and Ni co-doping, but the resulting HER performance depends on the balance between defect engineering and the intrinsic catalytic function of Ni species.

In summary, the Raman analysis serves two critical purposes in this study: (1) it confirms the successful modification of the carbon structure by N and Ni co-doping, and (2) it reveals that defect density alone cannot explain the observed HER activity trends, thereby highlighting the need to consider the complementary role of Ni-mediated water dissociation as the primary enhancement mechanism.

3.3.2 XPS analysis. The chemical states of elements in the catalysts were analyzed by XPS. The survey spectra (Fig. 7) confirm the presence of the respective elements and their valence state distributions.

High-resolution spectra were analyzed for Pt, N, C, and Ni (Fig. 8 and 9). The Pt 4f spectrum (Fig. 8a) shows characteristic peaks at 70.3 eV and 73.7 eV, corresponding to the $4f_{7/2}$ and $4f_{5/2}$ orbitals of metallic Pt (Pt^0), respectively. The binding energy ranges of 70.8–74.2 eV, 72.4–75.7 eV, and 74.0–77.2 eV are assigned to Pt^0, Pt^{2+}, and Pt^{4+} species, respectively. Based on peak area calculations, the proportions of $Pt^{\delta+}$ in Pt/TiO_2@3% Ni-N-C, Pt/TiO_2@1%Ni-N-C, and Pt/TiO_2@N-C catalysts are 53.5%, 48.0%, and 45.6%, respectively. This indicates that after NH_3 treatment, increasing the Ni doping content raises the proportion of Pt cations on the catalyst surface. The co-doping of N and Ni imparts a negative electron donor state to the catalyst surface, and the fitted Pt 4f spectrum exhibits a higher binding energy, confirming that N and Ni co-doping significantly alters the electronic structure of Pt.

The N 1s spectra (Fig. 8b) were deconvoluted into four components: pyridinic N (398.3 eV), pyrrolic N (399.8 eV), graphitic N (401.0 eV), and oxidized N (402.3 eV). Pyridinic and pyrrolic N atoms contribute one or two p electrons to the π-conjugated system. After Ni incorporation, the shape of the N 1s spectrum below 400 eV changes, showing a new peak at 399.7 eV attributed to the coordination between pyridinic N and Ni atoms. This new component slightly reduces the pyridinic N peak intensity, indicating the structural transformation of some pyridinic N atoms incorporated into the carbon lattice. In contrast, the electronic states and concentrations of graphitic N and pyrrolic N remain largely unchanged, suggesting that these species do not participate in Ni coordination and are less affected by the pyridinic N–Ni interaction.

As the Ni content increases, N atoms gradually replace graphitic C atoms at 401.7 eV, leading to a significant enhancement in the characteristic peak intensity of graphitic N. XPS analysis reveals that the binding energy of Ni 2p decreases with increasing Ni content, while the binding energy of N 1s shows a corresponding increase, confirming the strengthened N–Ni interaction. In the C 1s spectrum (Fig. 9a), characteristic peaks of four carbon species are observed at 284.0 eV (C═C), 284.9 eV (C–N), 286.5 eV (C–O), and 288.3 eV (C═O), confirming successful N doping *via* NH_3 treatment. This N doping not only enhances the surface adsorption capacity of the catalyst but also promotes the effective anchoring and stabilization of Ni atoms.

With increasing Ni doping, the content of C–N bonds decreases, indicating a reduction in the effective N doping level. As shown in Fig. 9b, Ni species exist mainly in three valence states: Ni^0 (852.2 eV), Ni^+ (853.8 eV), and Ni^{2+} (855.8 eV). Among these, Ni^+ serves as a key active site, effectively modulating the

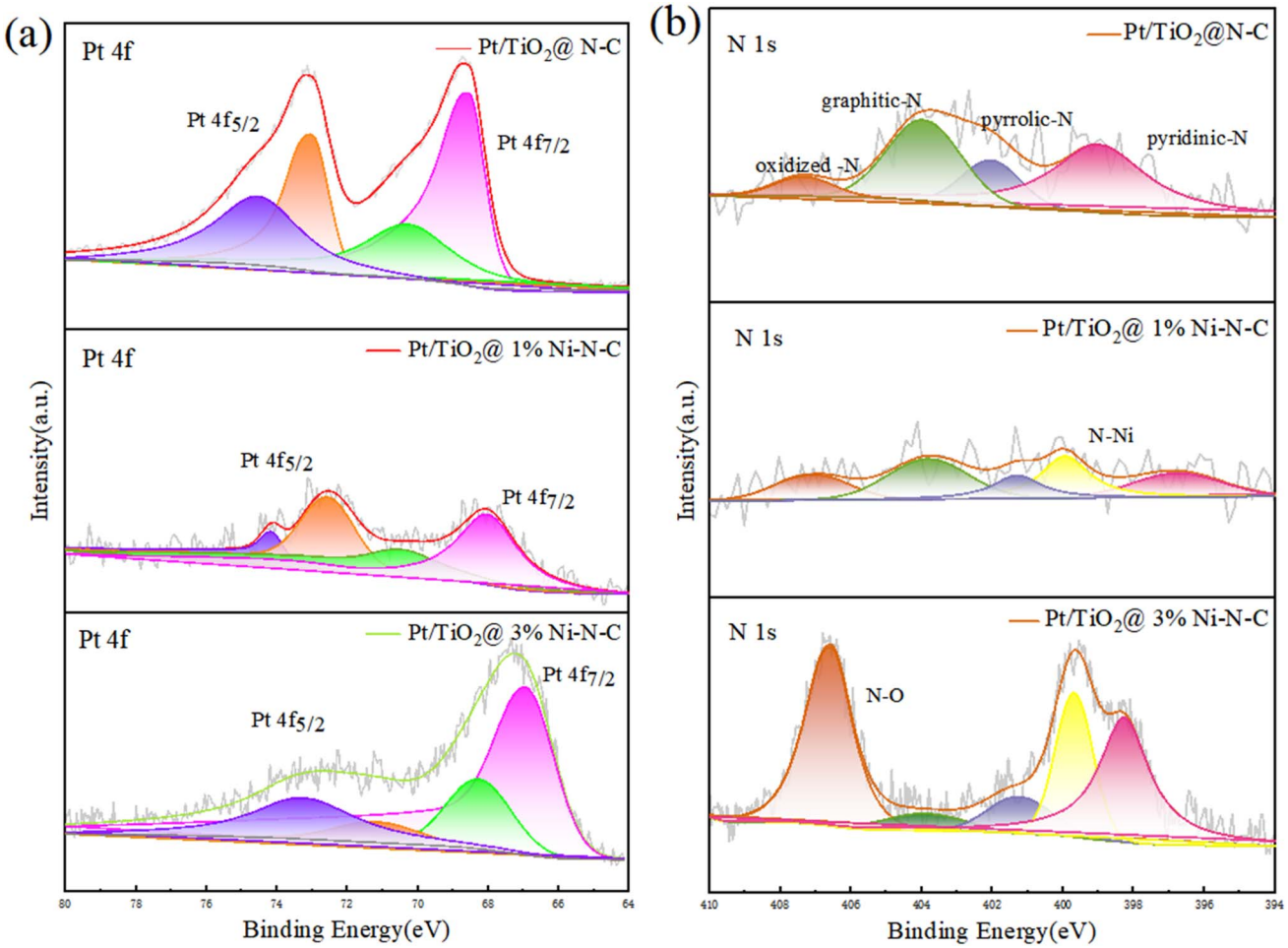

Fig. 8 High-resolution XPS spectra of Pt/TiO_2@3%Ni-N-C, Pt/TiO_2@1%Ni-N-C, and Pt/TiO_2@N-C catalysts: (a) Pt 4f, (b) N 1s.

electronic structure of surface Ni. Notably, the relative content of Ni^+ in Pt/TiO_2@1%Ni-N-C is higher than that in Pt/TiO_2@3% Ni-N-C, suggesting that a lower Ni doping amount is more conducive to the formation of Ni^+ active sites.

3.4 Catalytic performance of hydrogen evolution reaction

The HER activities of the catalysts were evaluated using multiple complementary electrochemical techniques. Linear sweep voltammetry (LSV) was employed to determine the overpotential required to achieve a current density of 10 mA cm^{-2}—the most commonly reported metric for HER activity, enabling direct comparison with literature values. Tafel analysis was conducted to probe reaction kinetics and elucidate the rate-determining step. Electrochemical impedance spectroscopy (EIS) was used to assess charge transfer resistance at the catalyst–electrolyte interface. Together, these three measurements provide a comprehensive and internally consistent assessment of HER performance. While direct quantification of hydrogen evolution rate would offer additional validation, the combination of overpotential, Tafel slope, and charge transfer resistance is widely accepted in the electrocatalysis community as sufficient for establishing relative activity trends and mechanistic insights.

The HER activities of the catalysts were evaluated using LSV at a scan rate of 5 mV s^{-1} in the potential range of −0.9 to −1.7 V (*vs.* Hg/HgO). The results are shown in Fig. 10a. Catalytic activity was compared based on the overpotential required to achieve a current density of 10 mA cm^{-2}. As seen in Fig. 10b, the overpotentials for Pt/TiO_2@1%Ni-N-C, Pt/TiO_2@N-C, and Pt/TiO_2@3%Ni-N-C are 84 mV, 117 mV, and 226 mV, respectively, all of which are lower than the 270 mV overpotential of the Pt/C catalyst prepared by the same method. Clearly, Pt/TiO_2@1%Ni-N-C exhibits the best HER performance.

The superior HER performance of Pt/TiO_2@1%Ni-N-C can be partly attributed to its optimized morphological features. The high specific surface area (108.9 m^2 g^{-1}) enables excellent dispersion of Pt nanoparticles, as confirmed by TEM analysis (Fig. 4), maximizing the number of accessible active sites. The mesoporous structure with pore sizes centered at 10–15 nm facilitates rapid diffusion of reactants to and products from the active sites, reducing concentration overpotentials. This morphological advantage is reflected in the low charge transfer resistance observed in EIS measurements (Fig. 10d). Notably, while Pt/TiO_2@3%Ni-N-C possesses an even higher surface area (135.2 m^2 g^{-1}), its slightly smaller average pore size (4.1 nm) and reduced defect density (as discussed in Section 3.3.1) may

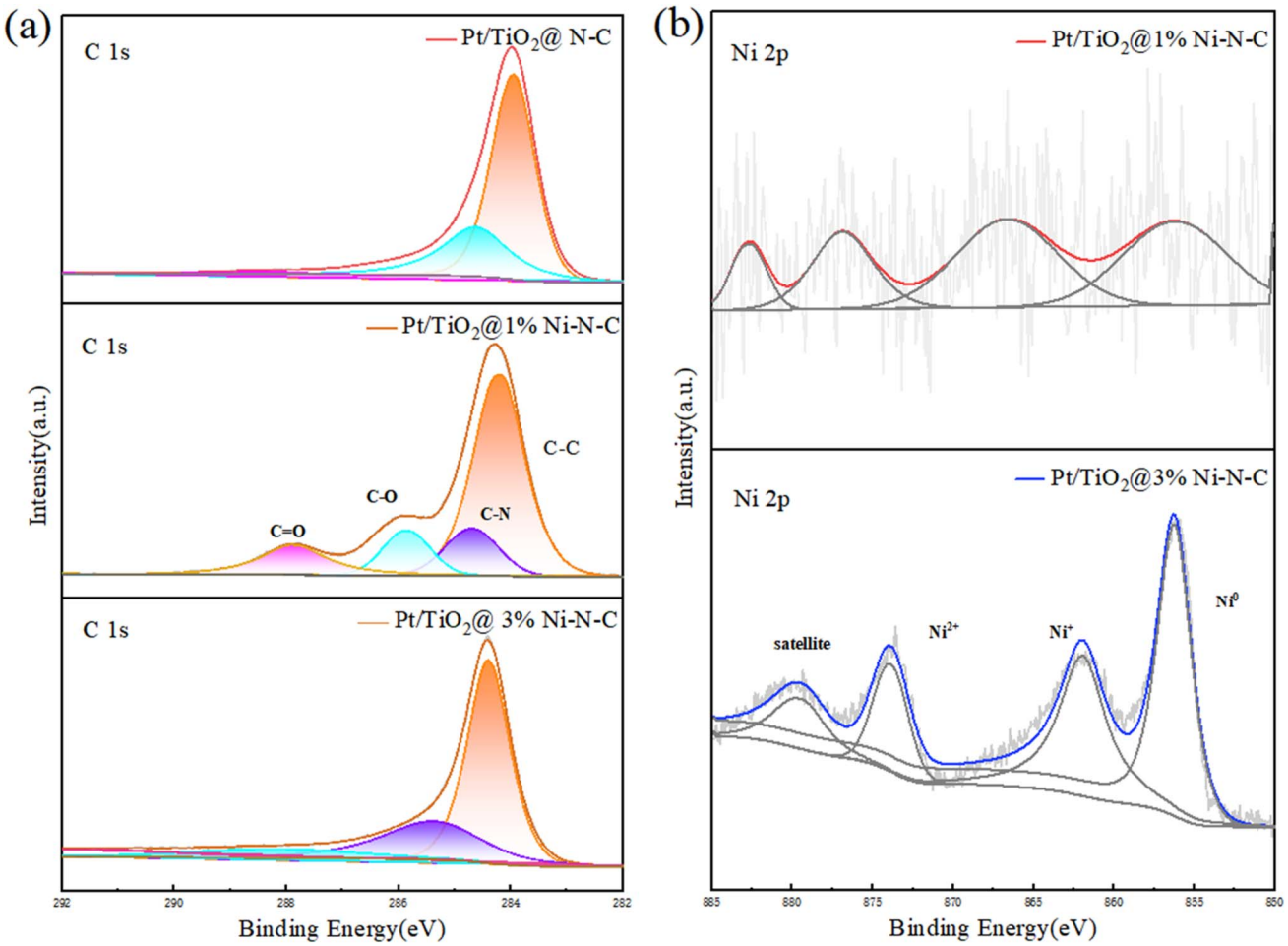

Fig. 9 High-resolution XPS spectra of Pt/TiO_2@3%Ni-N-C, Pt/TiO_2@1%Ni-N-C, and Pt/TiO_2@N-C catalysts: (a) C 1s, (b) Ni 2p.

hinder mass transport and active site accessibility, partially offsetting the benefit of increased surface area. These observations underscore that optimal HER performance requires not only high surface area but also an appropriate pore architecture and balanced electronic properties.

The LSV curves were further analyzed using the Tafel equation. The fitted Tafel slopes are presented in Fig. 10c. The Tafel slopes for Pt/TiO_2@1%Ni-N-C, Pt/TiO_2@3%Ni-N-C, and Pt/TiO_2@N-C are 115 mV dec^{-1}, 133 mV dec^{-1}, and 187 mV dec^{-1}, respectively. Pt/TiO_2@1%Ni-N-C possesses the smallest Tafel slope, indicating faster electron transfer kinetics and more favorable reaction kinetics.

Electrochemical impedance spectroscopy (EIS) was employed to compare the electrical conductivity of the catalysts. Impedance fitting was performed using the equivalent circuit shown in the inset of Fig. 10d. The Nyquist plots demonstrate that Pt/TiO_2@1%Ni-N-C has the lowest charge transfer resistance among the series, consistent with its highest HER rate.

3.5 Discussion on the catalytic mechanism

Dispersing Ni species on the TiO_2-modified N-doped carbon support enhances the catalyst's ability to adsorb and dissociate water molecules. Based on XRD analysis, we propose that during catalyst preparation, the addition of Ni induces structural changes in the polymeric carbon nitride within the support. As the Ni content increases, the polymeric carbon nitride converts into N-doped carbon, while highly dispersed Ni aggregates to form nanoparticles. Part of the Ni species is reduced by the carbon support during calcination. Ni incorporation induces charge redistribution within the support, and the unique heterointerfaces, combined with synergistic effects from functionalization, collectively enhance the catalyst's HER performance in alkaline media (Fig. 11).

Characterization results confirm the dominant role of Ni atoms in cleaving H–OH bonds. The HER activity of the catalyst can be tuned by rationally adjusting the Ni content. The Raman I_D/I_G ratios demonstrate that Ni doping has a non-linear effect on carbon defects: 1% Ni increases defect density, while 3% Ni reduces it below the level of the N-doped sample. This suggests that Ni at low loading may create additional structural distortions, while at high loading it promotes graphitization or surface coverage.

However, the HER performance does not scale linearly with defect density. Pt/TiO_2@3%Ni-N-C, despite having the fewest defects, still outperforms Pt/TiO_2@N-C. This clearly indicates

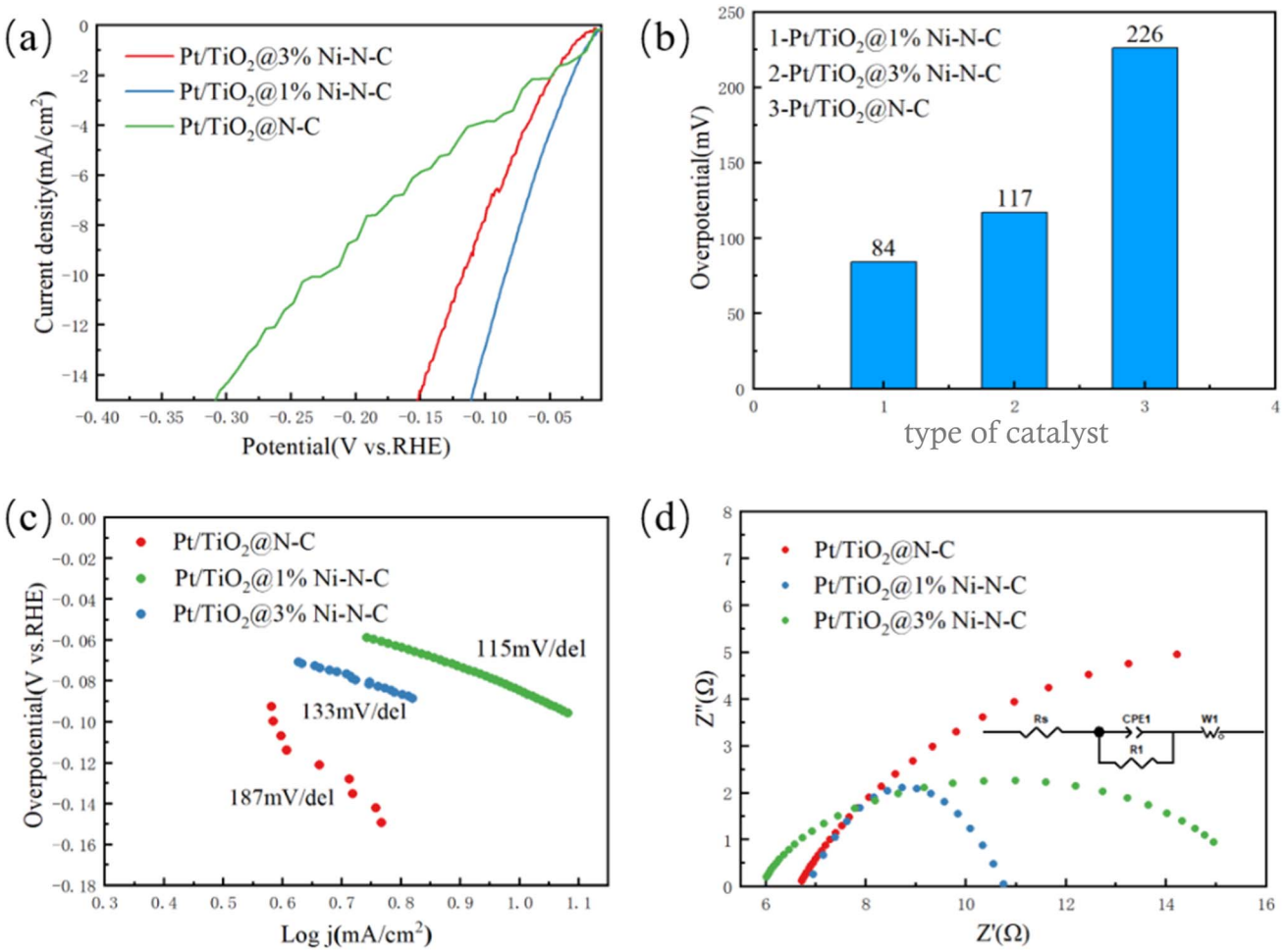

Fig. 10 HER performance of Pt/TiO_2@N-C, Pt/TiO_2@1%Ni-N-C, and Pt/TiO_2@3%Ni-N-C catalysts: (a) LSV curves, (b) overpotential comparison at 10 mA cm^{-2}, (c) Tafel plots, (d) Nyquist plots (inset: equivalent circuit).

that Ni's primary contribution is not through defect generation, but through its intrinsic ability to dissociate water molecules—a function that becomes increasingly effective with higher Ni loading up to an optimal point. The best performance of Pt/TiO_2@1%Ni-N-C represents the sweet spot where both contributions are maximized: sufficient defects to support Pt dispersion and electronic modulation, and an optimal amount of Ni^+ species (as confirmed by XPS) to facilitate the rate-determining Volmer step.

XPS analysis further supports this interpretation. The N and Ni co-doping imparts a negative electron donor state to the catalyst surface and increases the content of Pt cations. Oxidized Pt species can provide more catalytic active centers. Moreover, the doped N atoms primarily exist as pyridinic N, which not only donates electrons but also anchors Ni atoms, stabilizing the Ni^+ species that are identified as key active sites for water dissociation.

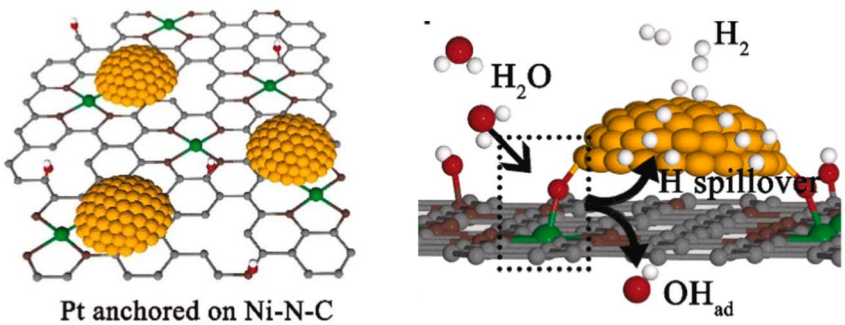

Fig. 11 Schematic illustration of Ni species cleaving the H–OH bond in water molecules within the catalyst.

The morphological evolution induced by Ni doping—particularly the creation of high-surface-area mesoporous structures—plays a crucial supporting role in the enhanced HER activity. This improved architecture not only accommodates better Pt dispersion but also ensures that the Ni^+ active sites identified by XPS are readily accessible to reactants. The optimal performance of Pt/TiO_2@1%Ni-N-C thus arises from a combination of favorable morphological features (high surface area with suitable mesopores), optimal Ni^+ content for water dissociation, and sufficient defect density for electronic modulation—a synergy that is disrupted when Ni loading is excessive.

4. Conclusions

In this study, a series of catalysts were successfully prepared by loading Pt species on n% Ni–N–C composites (n = 0, 1, 2). The composites, n% Ni–N–C, was synthesized by doping N into TiO_2-modified carbon supports *via* high-temperature NH_3 treatment Electrochemical tests demonstrated that Pt/TiO_2@1%Ni-N-C exhibited the optimal HER performance, with an overpotential of 84 mV and a Tafel slope of 115 mV dec^{-1}. All synthesized catalysts showed lower overpotentials than the Pt/C reference (270 mV), confirming that an appropriate amount of Ni doping significantly enhances its catalytic activity.

Through comprehensive characterization of the above-mentioned catalysts, the basic properties of these catalysts were elucidated. The uniform distributed Pt species, anatase TiO_2 phase, Ni species was present in XRD. With the increasing amount of Ni doping, the increased specific surface area while the reduced the pore size were shown.

Raman analysis indicated that N doping induces a redshift and correspondingly broadens the characteristic bands, along with a decrease in overall scattering intensity. The Raman spectral intensity decreases with increasing Ni content, while the degree of carbon disorder decreases only modestly. XPS analysis reveals that after NH_3 treatment, the content of cationic Pt on the catalyst surface increases with higher Ni doping levels.

In our view, N doping primarily enhances the stability of Ni species. And the strengthened interaction between pyridinic N and Ni facilitates the generation of Ni^+ species which serve as active sites for the hydrogen evolution reaction.

Looking forward, we recognize that direct quantification of hydrogen evolution rates would further strengthen the evaluation of catalyst performance. Future work in our laboratory will aim to establish the necessary experimental setup for gas collection and analysis, enabling more comprehensive kinetic studies and facilitating comparison with a broader range of catalytic systems.

Author contributions

Xufeng Lin: methodology, review and editing; project administration, funding acquisition. Huijie Wei: data curation, formal analysis, investigation, methodology, draft writing; Yixuan Zhang: data curation, formal analysis, review and editing; Hua Chi: formal analysis, investigation data curation; Xiaofan Liu: formal analysis, review and editing; Yanyan Xi: methodology, review and editing.

Conflicts of interest

The authors declare no competing financial interest.

Data availability

The data supporting this article have been included as part of the supplementary information (SI). Supplementary information: detailed catalyst characterization methods (XRD, N_2 adsorption–desorption, TEM, Raman, XPS), electrochemical measurement procedures for hydrogen evolution reaction (HER), and Fig. S1 (schematic diagram of the three-electrode system and its connection to the electrochemical workstation). See DOI: https://doi.org/10.1039/d6ra01906d.

Acknowledgements

Support from the National Natural Science Foundation of China (21576291) and from the Fundamental Research Funds for the Central Universities (23CX03007A) is gratefully acknowledged.

References

1 P. Achakulwisut, P. Erickson, C. Guivarch, R. Schaeffer, E. Brutschin and S. Pye, Global fossil fuel reduction pathways under different climate mitigation strategies and ambitions, *Nat. Commun.*, 2023, **14**, 5425–5439.
2 Y. Hui, M. Wang, S. Guo, S. Akhtar, S. Bhattacharya, B. Dai and J. Yu, Comprehensive review of development and applications of hydrogen energy technologies in China for carbon neutrality: Technology advances and challenges, *Energy Convers. Manage.*, 2024, **315**, 118776–118805.
3 K. K. Jaiswal, C. R. Chowdhury, D. Yadav, R. Verma, S. Dutta, K. S. Jaiswal, B. Sangmesh and K. S. K. Karuppasamy, Renewable and sustainable clean energy development and impact on social, economic, and environmental health, *Energy Nexus*, 2022, **7**, 100118–100131.
4 X. Pan, J. Qiu, S. Tang, Q. Lv, J. Dong, N. Jiang, L. Liu, Y. Wan, X. Yang, J. Han and F. Song, Engineering cobalt coordination environment with dual heteroatom doping for boosting urea-assisted hydrogen evolution, *Fuel*, 2025, **395**, 135161–135169.
5 H. Zhao and Z. Yuan, Engineering of transition metal phosphide-based heterostructures for electrocatalytic water splitting, *Smart Mater. Devices*, 2025, **1**, 202521–202539.
6 G. Fan, H. Zhang, B. Sun and F. Pan, Economic and environmental competitiveness of multiple hydrogen production pathways in China, *Nat. Commun.*, 2025, **16**, 4284–4299.
7 M. El-Shafie, Hydrogen production by water electrolysis technologies: A review, *Results Eng.*, 2023, **20**, 101426–101442.
8 J.-T. Ren, L. Chen, H.-Y. Wang, W.-W. Tian and Z.-Y. Yuan, Water electrolysis for hydrogen production: from hybrid

systems to self-powered/catalyzed devices, *Energy Environ. Sci.*, 2024, **17**, 49–113.

9 I. Barlocco, L. A. Cipriano, G. Di Liberto and G. Pacchioni, Does the Oxygen Evolution Reaction follow the classical OH*, O*, OOH* path on single atom catalysts?, *J. Catal.*, 2023, **417**, 351–359.

10 J. Li, Oxygen Evolution Reaction in Energy Conversion and Storage: Design Strategies Under and Beyond the Energy Scaling Relationship, *Nano–Micro Lett.*, 2022, **14**, 112–143.

11 K. Kodama, T. Nagai, A. Kuwaki, R. Jinnouchi and Y. Morimoto, Challenges in applying highly active Pt-based nanostructured catalysts for oxygen reduction reactions to fuel cell vehicles, *Nat. Nanotechnol.*, 2021, **16**, 140–147.

12 N. Bhuvanendran, S. Ravichandran, S. Lee, F. D. Sanij, S. Kandasamy, P. Pandey, H. Su and S. Y. Lee, Recent progress in Pt-based electrocatalysts: A comprehensive review of supported and support-free systems for oxygen reduction, *Coord. Chem. Rev.*, 2024, **521**, 216191–216235.

13 G. Gao, G. Zhu, X. Chen, Z. Sun and A. Cabot, Optimizing Pt-Based Alloy Electrocatalysts for Improved Hydrogen Evolution Performance in Alkaline Electrolytes: A Comprehensive Review, *ACS Nano*, 2023, **17**, 20804–20824.

14 J. Liang, H. Li, L. Chen, M. Ren, O. A. Fakayode, J. Han and C. Zhou, Efficient hydrogen evolution reaction performance using lignin-assisted chestnut shell carbon-loaded molybdenum disulfide, *Ind. Crops Prod.*, 2023, **193**, 116214–116226.

15 S. Samad, K. S. Loh, W. Y. Wong, T. K. Lee, J. Sunarso, S. T. Chong and W. R. Wan Daud, Carbon and non-carbon support materials for platinum-based catalysts in fuel cells, *Int. J. Hydrogen Energy*, 2018, **43**, 7823–7854.

16 Z.-d Wang, T. Xia, Z.-h Li and M.-f Shao, A review of carbon-based catalysts and catalyst supports for simultaneous organic electro-oxidation and hydrogen evolution reactions, *New Carbon Mater.*, 2024, **39**, 67–77.

17 Y. Da, X. Li, Y. Wang, G. Xie, S. Liu, L. Zhang, H. Liang, Y. Li and B. Wang, Recent advances of heteroatom-doped carbon-based materials: Synthesis, properties, environmental application, and catalytic mechanism in advanced oxidation processes, *J. Water Process Eng.*, 2025, **76**, 108286–108310.

18 M. Inagaki, M. Toyoda, Y. Soneda and T. Morishita, Nitrogen-doped carbon materials, *Carbon*, 2018, **132**, 104–140.

19 J. L. Fiorio, M. A. S. Garcia, M. L. Gothe, D. Galvan, P. C. Troise, C. A. Conte-Junior, P. Vidinha, P. H. C. Camargo and L. M. Rossi, Recent advances in the use of nitrogen-doped carbon materials for the design of noble metal catalysts, *Coord. Chem. Rev.*, 2023, **481**, 215053–215081.

20 S. Kaushal and J. Andrews, A review on the nitrogenated carbon materials and their electrochemical performance for energy storage applications, *Int. J. Hydrogen Energy*, 2025, **100**, 1231–1245.

21 D. Salinas-Torres, M. Navlani-García, K. Mori, Y. Kuwahara and H. Yamashita, Nitrogen-doped carbon materials as a promising platform toward the efficient catalysis for hydrogen generation, *Appl. Catal., A*, 2019, **571**, 25–41.

22 T. W. van Deelen, C. Hernández Mejía and K. P. de Jong, Control of metal-support interactions in heterogeneous catalysts to enhance activity and selectivity, *Nat. Catal.*, 2019, **2**, 955–970.

23 L. F. Mabena, S. Sinha Ray, S. D. Mhlanga and N. J. Coville, Nitrogen-doped carbon nanotubes as a metal catalyst support, *Appl. Nanosci.*, 2011, **1**, 67–77.

24 B. Zhang, S. Yu, Y. Dai, X. Huang, L. Chou, G. Lu, G. Dong and Y. Bi, Nitrogen-incorporation activates $NiFeO_x$ catalysts for efficiently boosting oxygen evolution activity and stability of $BiVO_4$ photoanodes, *Nat. Commun.*, 2021, **12**, 6969–6976.

25 B. Li, L. Zhang, J. Zhang and Y. Su, Recent Insight in Transition Metal Anchored on Nitrogen-Doped Carbon Catalysts: Preparation and Catalysis Application, *Electrochem*, 2022, **3**, 520–537.

26 Z. Qiao, S. Hwang, X. Li, C. Wang, W. Samarakoon, S. Karakalos, D. Li, M. Chen, Y. He, M. Wang, Z. Liu, G. Wang, H. Zhou, Z. Feng, D. Su, J. S. Spendelow and G. Wu, 3D porous graphitic nanocarbon for enhancing the performance and durability of Pt catalysts: a balance between graphitization and hierarchical porosity, *Energy Environ. Sci.*, 2019, **12**, 2830–2841.

27 Q. Pang, X. Fan, K. Sun, K. Xiang, B. Li, S. Zhao, Y. D. Kim, Q. Liu, Z. Liu and Z. Peng, Nickel–Nitrogen–Carbon (Ni–N–C) Electrocatalysts Toward CO_2 electroreduction to CO: Advances, Optimizations, Challenges, and Prospects, *Energy Environ. Mater.*, 2024, **7**, 12731–12931.

28 K. Mainali, S. H. Mood, M. R. Pelaez-Samaniego, V. Sierra-Jimenez and M. Garcia-Perez, Production and applications of N-doped carbons from bioresources: A review, *Catal. Today*, 2023, **423**, 114248–114268.

29 W. Al-Hajri, Y. De Luna and N. Bensalah, Review on Recent Applications of Nitrogen-Doped Carbon Materials in CO_2 Capture and Energy Conversion and Storage, *Energy Technol.*, 2022, **10**, 220498–220515.

30 W. Ni, J. L. Meibom, N. U. Hassan, M. Chang, Y.-C. Chu, A. Krammer, S. Sun, Y. Zheng, L. Bai, W. Ma, S. Lee, S. Jin, J. S. Luterbacher, A. Schüler, H. M. Chen, W. E. Mustain and X. Hu, Synergistic interactions between PtRu catalyst and nitrogen-doped carbon support boost hydrogen oxidation, *Nat. Catal.*, 2023, **6**, 773–783.

31 J. Wen, S. Tang, X. Ding, Y. Yin, F. Song and X. Yang, In Situ Raman Study of Layered Double Hydroxide Catalysts for Water Oxidation to Hydrogen Evolution: Recent Progress and Future Perspectives, *Energies*, 2024, **17**, 5712.

32 T. Yoshii, G. Nishikawa, V. K. Prasad, S. Shimizu, R. Kawaguchi, R. Tang, K. Chida, N. Sato, R. Sakamoto, K. Takatani, D. Moreno-Rodríguez, P. Škorňa, E. Scholtzová, R. K. Szilagyi and H. Nishihara, Quantitative and qualitative analysis of nitrogen species in carbon at the ppm level, *Chem*, 2024, **10**, 2450–2463.

33 Y. Shang, Y. Ding, P. Zhang, M. Wang, Y. Jia, Y. Xu, Y. Li, K. Fan, L. Sun, N. Pyrrolic and N. or pyridinic, The active

center of N-doped carbon for CO_2 reduction, *Chin. J. Catal.*, 2022, **43**, 2405–2413.

34 J. Zhang, G. Zhang, S. Jin, Y. Zhou, Q. Ji, H. Lan, H. Liu, J. Qu and N. Graphitic, in nitrogen-Doped carbon promotes hydrogen peroxide synthesis from electrocatalytic oxygen reduction, *Carbon*, 2020, **163**, 154–161.

35 Q. Lv, W. Si, J. He, L. Sun, C. Zhang, N. Wang, Z. Yang, X. Li, X. Wang, W. Deng, Y. Long, C. Huang and Y. Li, Selectively nitrogen-doped carbon materials as superior metal-free catalysts for oxygen reduction, *Nat. Commun.*, 2018, **9**, 3376–3386.

36 Y. Xu, Y. Mo, J. Tian, P. Wang, H. Yu and J. Yu, The synergistic effect of graphitic N and pyrrolic N for the enhanced photocatalytic performance of nitrogen-doped graphene/TiO_2 nanocomposites, *Appl. Catal., B*, 2016, **181**, 810–817.

37 H. Yang, H. Wang, L. Wang, M. Sun, F. Xu, H. Ye, J. Ren and Z. Yuan, Optimized electronic structure induced by cobalt metaphosphate/phosphide for highly efficient hydrazine-assisted water splitting at high current densities, *J. Colloid Interface Sci.*, 2025, **695**, 137765–137772.

38 D. Li, L. Ding, Q. Zhao, F. Yang and S. Zhang, Controllable construction of bifunctional sites on Ir@Ni/NiO core/shell porous nanorod arrays for efficient water splitting, *Appl. Energy*, 2024, **356**, 122369–122378.

39 K. Dastafkan, X. Shen, R. K. Hocking, Q. Meyer and C. Zhao, Monometallic interphasic synergy via nano-hetero-interfacing for hydrogen evolution in alkaline electrolytes, *Nat. Commun.*, 2023, **14**, 547–556.

40 L. Du, L. B. Chen, X. Liu, C. Yang and Q. Jiang, Heterogeneous interface and vacancy engineering contribute to metastable catalysts for overall water splitting, *Acta Mater.*, 2025, **289**, 120934–120945.

41 X. Tian, R. Ren, F. Wei, J. Pei, Z. Zhuang, L. Zhuang and W. Sheng, Metal-support interaction boosts the stability of Ni-based electrocatalysts for alkaline hydrogen oxidation, *Nat. Commun.*, 2024, **15**, 76–88.

42 L. Li, X. Cao, J. Huo, J. Qu, W. Chen, C. Liu, Y. Zhao, H. Liu and G. Wang, High valence metals engineering strategies of Fe/Co/Ni-based catalysts for boosted OER electrocatalysis, *J. Energy Chem.*, 2023, **76**, 195–213.

43 C. Lim, A. R. Fairhurst, B. J. Ransom, D. Haering and V. R. Stamenkovic, Role of Transition Metals in Pt Alloy Catalysts for the Oxygen Reduction Reaction, *ACS Catal.*, 2023, **13**, 14874–14893.

44 H. Osgood, S. V. Devaguptapu, H. Xu, J. Cho and G. Wu, Transition metal (Fe, Co, Ni, and Mn) oxides for oxygen reduction and evolution bifunctional catalysts in alkaline media, *Nano Today*, 2016, **11**, 601–625.

45 L. Huang, N. Wang, M. Qi, Z. Liu, Z. Xu, Q. Zhang, Z. Shu, S. Shan, Y. Bian, J. Chen and Y. Jiao, The strong metal-support interaction at Ni–O–Pt interface facilitates rapid electrocatalytic hydrogen production, *Int. J. Hydrogen Energy*, 2024, **88**, 1217–1225.